



Contents lists available at ScienceDirect

# Geochimica et Cosmochimica Acta

journal homepage: [www.elsevier.com/locate/gca](http://www.elsevier.com/locate/gca)



## Rates of dehydration in hydrous, high-Fo, magmatic olivines

Anna Barth<sup>a,\*</sup>, Terry Plank<sup>b</sup>, Henry Towbin<sup>b</sup>

<sup>a</sup> University of California, Berkeley, United States

<sup>b</sup> Lamont-Doherty Earth Observatory, United States



### ARTICLE INFO

#### Article history:

Received 13 May 2022

Accepted 13 November 2022

Available online 19 November 2022

Associate editor: James Van Orman

### ABSTRACT

Natural olivine from the Etna Fall Stratified eruption (3930 BP) was dehydrated to determine hydrogen diffusivity. Dehydration was carried out in several time-steps, from 0.5 to 40 cumulative hours, in a 1 atm. furnace at 810 and 1000 °C. This starting material has high H<sub>2</sub>O concentration (~50 ppm), high forsterite (Fo ~ 90 %), and high *f*O<sub>2</sub> (~NNO + 1.2), reflecting characteristics of its host magma. H<sub>2</sub>O concentration was measured using Fourier transform infrared spectroscopy after each heating step. Spectral peaks were fit with Gaussian curves to determine the contribution from each H<sup>+</sup> defect. Zonation profiles along each crystallographic direction were modelled using the ‘whole-block’ method to determine bulk and defect-specific H<sup>+</sup> diffusivity.

Our modelling reveals a common apparent diffusivity for all defects, which is faster along ([100]) than **b** ([010]) or **c** ([001]) by more than an order of magnitude. A common defect-specific diffusivity has not been found in experiments on pure forsterite, so it appears that the presence of Fe enables H<sup>+</sup> from all defects to diffuse via the proton-polaron mechanism (supported by the observed anisotropy). However, the rates that we observe are slower than the proton-polaron mechanism, which supports the recent proposal by Ferriss et al. (2018) that the apparent diffusivity is rate-limited by reactions between H<sup>+</sup> bound in defect sites and Fe<sup>2+</sup>. A coupled reaction and diffusion process may explain the observed decrease in diffusivity along **a** over time, as well as an apparent non-zero H<sub>2</sub>O concentration at the crystal edge. Both of these effects need to be considered when modelling H<sup>+</sup> diffusion profiles to determine decompression rate – fixing the edge concentration to zero will underestimate the diffusion timescale.

Arrhenius laws describing diffusion parallel to **a** (at the start and end of the experiments), **b**, and **c** are developed from the diffusivity at 810 and 1000 °C:  $D_{a\text{start}} = 10^{-2.94} \exp\left(\frac{-182000}{RT}\right)$ ,  $D_{a\text{end}} = 10^{-4.63} \exp\left(\frac{-154000}{RT}\right)$ ,  $D_b = 10^{-2.35} \exp\left(\frac{-243000}{RT}\right)$ ,  $D_c = 10^{-4.01} \exp\left(\frac{-187000}{RT}\right)$ , where *R* is the gas constant 8.314 (J/mol K); *T* is the temperature (K), the units of the diffusivities (*D*) are in m<sup>2</sup>/s. A comparison of experimental dehydration studies on natural olivines reveals that the diffusivity during dehydration likely depends on how the olivine was experimentally hydrated. To avoid this experimental effect and understand the diffusivity operating during ascent in a volcanic conduit, crystals which are naturally hydrous (such as the Etna olivines in this study) are particularly useful. Despite some ambiguity in the literature owing to different experimental approaches, our results suggest that for the studied range of pressure and temperature, forsterite content is the major control on H<sup>+</sup> diffusivity, while H<sub>2</sub>O concentration and the *f*O<sub>2</sub> at which the crystal last equilibrated have a smaller effect within the ranges studied for magmatic olivines.

© 2022 Elsevier Ltd. All rights reserved.

### 1. Introduction

The diffusivity of hydrogen in olivine has implications for a broad range of processes in the earth sciences. Although olivine is nominally anhydrous, it can store hundreds of ppm H<sub>2</sub>O through defects in its lattice – enough to significantly affect the strength of olivine and consequently the rheology of the mantle (Beran, 1969; Bai and Kohlstedt, 1992; Bell and Rossman, 1992; Faul et al., 2016).

H<sup>+</sup> diffusivity (i.e., the movement of protons) in olivine is also related to olivine's electrical conductivity (i.e., the movement of electrons), which can provide constraints on the presence of water and melt in the mantle (Karato, 1990; Yoshino et al., 2006; Novella et al., 2017). Another application of H<sup>+</sup> diffusion in olivine is as a chronometer for magma decompression rate during volcanic eruptions (Demouchy et al., 2006; Newcombe et al., 2020). As magma ascends in the conduit it degasses H<sub>2</sub>O into vapour bubbles, which causes the outwards diffusion of H<sup>+</sup> from crystals carried within the host magma. If the diffusivity of H<sup>+</sup> in olivine is known, the resulting diffusion profiles can be modelled to determine the

\* Corresponding author.

E-mail address: [barthac@berkeley.edu](mailto:barthac@berkeley.edu) (A. Barth).

decompression rate of the magma, a critical parameter that relates to volcanic explosivity (Cassidy et al., 2018; Barth et al., 2019).

The incorporation of water into olivine occurs through point defects in the lattice and is governed by charge balance. For example, a  $\text{Si}^{4+}$  vacancy may be charge balanced by  $4\text{H}^+$ . The O–H bonds in these different defects absorb energy in the infrared range and so can be observed using Fourier transform infrared (FTIR) spectroscopy (Beran and Putnis, 1983; Berry et al., 2005, 2007). The wavelength of an absorption peak in FTIR spectra is indicative of the type of defect. Studies using FTIR spectroscopy have found that the most common defects in natural olivines are as follows:  $2\text{H}^+$  charge balancing a metal $^{2+}$  vacancy [Mg];  $\text{H}^+$  charge balancing a metal $^{2+}$  vacancy and a trivalent ion ( $\text{Fe}^{3+}$ ,  $\text{Al}^{3+}$ ,  $\text{Cr}^{3+}$ ) substituting on a metal site [Triv]; and  $2\text{H}^+$  charge balancing a  $\text{Si}^{4+}$  vacancy and a  $\text{Ti}^{4+}$  on a metal site [Ti] (Matveev et al., 2001; Lemaire et al., 2004; Padrón-Navarta et al., 2014; Blanchard et al., 2017; Ferriss et al., 2018). Note, that for discussion of water concentration we use  $\text{H}_2\text{O}$  wt. % ppm, while for diffusion or defects we refer to water as  $\text{H}^+$ .

Experiments using San Carlos olivine have revealed two primary diffusion mechanisms in natural olivines (Mackwell and Kohlstedt, 1990; Kohlstedt and Mackwell, 1998; Demouchy and Mackwell, 2006). The faster mechanism involves a flux of  $\text{H}^+$  charge-balanced by a flux of electrons from  $\text{Fe}^{2+}$  to  $\text{Fe}^{3+}$ .  $\text{Fe}^{3+}$  and their associated electron holes in the metal site vacancies create defects called polarons, and so this diffusion mechanism is often referred to as the proton-polaron mechanism. The second, slower mechanism involves the diffusion of metal vacancies along with their associated  $\text{H}^+$  and is called the proton-vacancy mechanism. Just like Mg-Fe diffusion, this mechanism is fastest along the  $\underline{c}$  direction, [001], whereas proton-polaron is fastest along  $\underline{a}$ , [100] (Kohlstedt and Mackwell, 1998; Dohmen et al., 2007).

Since both proton-polaron and proton-vacancy mechanisms involve the exchange of two components (protons and polarons, protons and vacancies) there is an ‘exchange’ diffusivity which depends on the individual diffusivity of each exchanging species:

$$D_{\text{exchange}}^{\text{pp}} = \frac{2D_{\text{H}}D_{\text{p}}}{D_{\text{H}} + D_{\text{p}}} \quad (1a)$$

$$D_{\text{exchange}}^{\text{pv}} = \frac{3D_{\text{V\_Me}}D_{\text{p}}}{2D_{\text{V\_Me}} + D_{\text{p}}} \quad (1b)$$

where,  $D_{\text{p}}$  is the polaron diffusivity,  $D_{\text{H}}$  is the proton diffusivity, and  $D_{\text{V\_Me}}$  is the metal vacancy diffusivity. Since  $D_{\text{p}} \gg D_{\text{H}} \gg D_{\text{V\_Me}}$ , these expressions can be simplified to  $D_{\text{exchange}}^{\text{pp}} = 2D_{\text{H}}$  and  $D_{\text{exchange}}^{\text{pv}} = 3D_{\text{V\_Me}}$  (Kohlstedt and Mackwell, 1998). This has led to some confusion in the literature – the diffusivity responsible for generating diffusion profiles is the ‘exchange diffusivity’. However, the Arrhenius figures in Kohlstedt and Mackwell (1998) (their Figs. 3, 4, 6) instead illustrate the individual species’ diffusivities (e.g.  $D_{\text{H}}$ ), which is a factor of 2 and 3 slower than the exchange diffusivity, for proton-polaron and proton-vacancy diffusion, respectively. Some studies (e.g. Ferriss et al., 2018) compare results to these diffusivities for individual species (e.g.  $D_{\text{H}}$ ), when instead they should be compared to the ‘exchange diffusivity’ ( $D_{\text{exchange}}^{\text{pp}}$ ). In this paper, all discussion of the proton-polaron or proton-vacancy rates will be based on the exchange diffusivity (e.g.  $D_{\text{exchange}}^{\text{pp}}$ ), since this is the diffusivity that is obtained directly from modelling experimentally generated diffusion profiles.

Recent studies have shown that  $\text{H}^+$  diffusion in natural volcanic olivine is fastest along  $\underline{a}$ , yet slower than the proton-polaron rate (Ferriss et al., 2018; Barth et al., 2019; Jollands et al., 2019). One explanation put forward by Ferriss et al. (2018) and Jollands et al. (2019) is that the  $\text{H}^+$  located in defect sites must first undergo

a reaction before diffusing through the crystal at the proton-polaron rate. This extra reaction step decreases the ‘apparent’ diffusivity from the true proton-polaron diffusivity. In this paper, we use the term ‘apparent diffusivity’ to describe the combined effects of diffusion and defect reactions.

The rate of these reactions is set by the crystal defect structure and so may vary between olivines of different chemistry. For example, the faster apparent  $\text{H}^+$  diffusivities in Fo ~ 80 olivines from Cerro Negro volcano compared to San Carlos and Kilauea olivines (Fo ~ 90) were attributed to the olivine’s higher Fe content (Barth et al., 2019). In addition to the concentration of Fe, the relative amount of  $\text{Fe}^{3+}$  and  $\text{Fe}^{2+}$  (which is affected by the  $f\text{O}_2$  at which the olivines last equilibrated) is also thought to affect  $\text{H}^+$  diffusivity in olivine. Ferriss et al. (2018) observe faster apparent diffusivity in olivines from San Carlos than from Kilauea, which they suggest may be related to the oxygen fugacity at which the olivines equilibrated. The  $\text{H}_2\text{O}$  concentration itself may also affect the rate of these reactions. Jollands et al. (2019) find significantly lower apparent diffusivities in olivine with higher  $\text{H}_2\text{O}$  concentrations, despite the olivines having similar forsterite and trace element contents. They argue that a higher ratio of  $\text{H}^+$  to trace elements limits the availability of defects available to react with  $\text{H}^+$ , thereby lowering the apparent diffusivity. However, the olivines used in these experiments were metamorphic and contained far more  $\text{H}_2\text{O}$  (~150 ppm) than observed in magmatic olivines (generally < 100 ppm).

To explore these proposed compositional effects (forsterite,  $\text{H}_2\text{O}$  concentration,  $f\text{O}_2$  of equilibration), we carry out dehydration experiments on a natural olivine phenocryst from the 3930 BP subplinian Etna Fall Stratified eruption (Coltelli et al., 2005; Kamenetsky et al., 2007). Samples from this eruption contain many clear, euhedral, and large (>1 mm) olivines that are ideal for experimentation. Furthermore, olivine-hosted melt inclusions from this deposit indicate that the magma was water-rich (4–5 wt%  $\text{H}_2\text{O}$ ) and oxidized (NNO + 1.2) at depth (Kamenetsky et al., 2007; Gennaro et al., 2020), while having similarly high Fo (Fo 90) as the Kilauea and San Carlos olivines studied in Ferriss et al. (2018) (Fo 86 and 88, respectively). These characteristics make the Etna Fall Stratified olivine a good candidate for comparing the relative effects of forsterite,  $f\text{O}_2$ , and  $\text{H}_2\text{O}$  concentration on  $\text{H}^+$  diffusivity in olivine. In addition, the high  $\text{H}_2\text{O}$  concentrations in the olivines (~40 ppm) means that we do not need to experimentally hydrate the olivines, which allows us to avoid any changes to the crystal defect structure prior to dehydration. The  $\text{H}^+$  diffusivities determined here also provide the basis for an accurate speedometer with which to quantify decompression rates for the explosive Fall Stratified eruption of Etna (Barth, 2021).

## 2. Methods

### 2.1. Sample preparation

A single Etna Fall Stratified olivine from sample IGSN: IEACB000Y was cut in two and both halves polished into cuboids (ETFS-block1 and ETFS-block2 – see Fig. 1). Sample thicknesses in all three crystallographic directions were measured with a digital micrometer accurate to within 5  $\mu\text{m}$ , and are  $953 \times 670 \times 1246$  and  $953 \times 725 \times 1246$   $\mu\text{m}$  for blocks 1 and 2, respectively. Crystallographic directions were determined from crystal morphology and confirmed with electron backscatter diffraction (EBSD). Several hundred microns were polished off the rims, with the goal of removing rims with low concentration of  $\text{H}_2\text{O}$  (a ubiquitous feature of olivine phenocrysts, Newcombe et al. (2020)): the resulting initial  $\text{H}_2\text{O}$  profiles are broadly homogeneous along  $\underline{a}$  (within 6 % for block1, 8.1 % for block2), apart from the [Mg] peak which shows

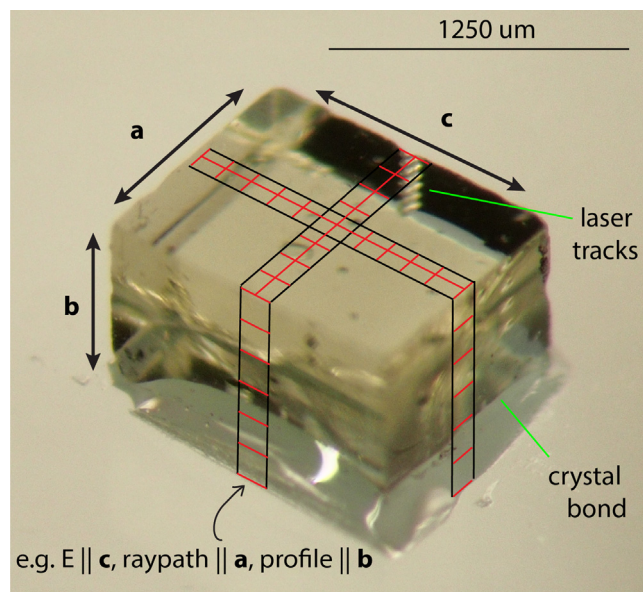


**Fig. 1.** Photo of Etna FS block 2 showing configuration of FTIR profiles. Red lines indicate electric polarization direction, E. Any blemishes in the photo are due to crystal bond (which the crystal is mounted in) and laser tracks – neither olivine blocks have inclusions or internal fractures. Below olivine, notation is shown for example profile along **b** on the **a** face.

16 % variation along **a** for block2. Profiles along **b** and **c** for block1 show more variability – up to 30 % for the [Mg] peak (Figure S1, Figure S2).

## 2.2. Laser Ablation ICP-MS

Laser ablation ICP-MS traverses were conducted to measure  $^{26}\text{Mg}$ ,  $^{29}\text{Si}$ ,  $^{31}\text{P}$ ,  $^{43}\text{Ca}$ ,  $^{45}\text{Sc}$ ,  $^{47}\text{Ti}$ ,  $^{52}\text{Cr}$ ,  $^{55}\text{Mn}$ ,  $^{57}\text{Fe}$ ,  $^{59}\text{Co}$ ,  $^{60}\text{Ni}$ , and  $^{66}\text{Zn}$  using a Thermo/VG PQ ExCell and ESI 193 nm excimer laser at the Lamont-Doherty Earth Observatory (LDEO) after all experiments were complete. The crystals were rastered from edge to edge of the olivine cuboids at 3  $\mu\text{m/s}$  using a 25  $\mu\text{m}$  spot size, 15 Hz, and 2.4  $\text{GW/cm}^2$  following a pre-ablation step to clean the sample surface. Background was collected for 1 min with the laser firing at the shutter. The average background was subtracted from the signal, which was then averaged in blocks of 20 points. Initial counts were calibrated using the BIR-1 g glass (values in Kelley et al., 2003), and some elements were corrected to the certified values for San Carlos olivine (Jarosewich et al., 1980). Measured profiles show limited zonation (<10 %, Table S1).

## 2.3. Dehydration experiments

Both blocks were heated at 1 atm in increments using a vertical furnace (described in Ferriss et al., 2015), with oxygen fugacity held at  $\text{NNO} + 1.2$  (Gennaro et al., 2020) by mixing  $\text{CO-CO}_2$  gas. ETFS-block1 was heated at 810  $^\circ\text{C}$  and an oxygen fugacity of  $10^{-12.5}$  bars for 0.5, 2, 5, 8, 12, 26 and 40 cumulative hours. ETFS-block2 was heated at 1000  $^\circ\text{C}$  and an oxygen fugacity of  $10^{-9.2}$  bars for 0.5, 1, 2, and 4 cumulative hours.

## 2.4. FTIR Spectroscopy

Olivine water concentrations were measured through the whole blocks (Ferriss et al., 2015) using Fourier transform infrared (FTIR) spectroscopy. Spectra were collected using the Thermo Nicolet Nexus 670 infrared spectrometer and Thermo Nicolet Continuum

15x infrared microscope at American Museum of Natural History with a Globar source and KBr beamsplitter for MIR light. Measurements were collected with an aperture of  $100 \times 100 \mu\text{m}$  (although the actual sampled volume will be larger due to focusing of the beam within the olivine crystal), resolution of  $4 \text{ cm}^{-1}$ , and averaged over 200 scans. We fit a quadratic baseline through the spectra between wavenumbers 3100 and  $3650 \text{ cm}^{-1}$ . After subtracting this baseline, we fit Gaussian peaks with fixed positions and widths (Table 1) to the spectra to determine defect-specific  $\text{H}_2\text{O}$  concentration profiles based on peak areas. We calculate absolute water concentrations with the calibration of Withers et al. (2012), although the results of diffusion modelling are only sensitive to relative differences in water concentrations and so the choice of calibration has no bearing on the calculated diffusivities.

Between each heating step,  $\text{H}_2\text{O}$  profiles were measured with a Thermo Nicolet wire ZnSe polarizer parallel to crystallographic axes. For each crystallographic direction, a profile was measured with the electric vector, E, polarized along **a** and **c** (Fig. 1). Each analysis represents an average water concentration along the path of the infrared beam (i.e., through the “whole block”), and an orthogonal series of such measurements can be used to determine the diffusivities along each crystallographic direction, as described in Ferriss et al. (2015).

## 2.5. Modelling diffusion profiles

Because of the path-integrated 3D nature of the FTIR profiles, there are various trade-offs between the diffusivity along **a**, **b**, and **c**, as well as the  $\text{H}_2\text{O}$  concentration at the crystal edge (which typically appears to be above zero – see section 4.3). For each diffusion profile, we find the best-fit values for these parameters that minimizes the misfit between the data and the model using the python package `scipy.optimize.minimize` (Virtanen et al., 2020). Misfit is calculated as the square of the difference between the  $\text{H}_2\text{O}$  concentration predicted by the whole-block forward diffusion model from (Ferriss et al., 2018) and that measured by FTIR spectroscopy, summed for all data points along all profiles (**a**, **b**, **c**). Note that because we model diffusion from the initial profile to the profile at each time-step, temporal variation in diffusivity is averaged over the entire time interval. Therefore, any temporal variations that we observe would in fact be magnified in reality. For example, to model the diffusion profiles generated after 40 h of heating at 810  $^\circ\text{C}$ , we use the profile at time zero for the initial and a time interval of 40 h, rather than the profile at 26 h with a time interval of 14 h. This time-integration smoothing effect is a necessary result of requiring an analytical solution for the whole-block diffusion modelling, which requires a uniform concentration profile as a starting condition, i.e. we cannot use diffusion profiles generated at time  $t$  as the initial profile for modelling diffusion at time  $t + 1$ .

To assess uncertainty in the free parameters ( $D_a$ ,  $D_b$ ,  $D_c$ , edge concentration), we perform Markov Chain Monte Carlo (MCMC) simulations to explore the parameter space around the best-fit

**Table 1**

Positions and widths of modelled peaks. Peak positions are similar to those reported in Berry et al., 2005; Berry et al., 2007; Padrón-Navarta et al., 2014.

Peak wavenumber $\text{cm}^{-1}$	Peak width $\text{cm}^{-1}$	Interpreted defect
3232	78	[Mg]
3329	29	[triv]
3359	20	[triv]
3524	32	[Ti]
3546	12	[Si]
3559	11	[Si]
3573	14	[Ti]
3600	24	[Si]



values. We use the python package ‘mc3’ with a ‘Snooker’ sampling method (Ter Braak and Vrugt, 2008; Cubillos et al., 2016) and 10,000 samples (discarding the first 500 samples). In most cases, we use the best-fit values as the starting parameters, however in some instances, the least squares optimisation did not provide a meaningful result (when the parameter was poorly constrained) and for these cases we set the initial parameter manually:  $\log_{10}(D_b)$  and  $\log_{10}(D_c)$  at 1000 °C were set to  $-12$ , and  $\log_{10}(D_b)$  at 810 °C was set to  $-13$ . The upper and lower bounds on parameters ( $P_{min}$  and  $P_{max}$ ) were held constant for all time-steps and chosen to encompass all plausible results (although note that in some instances – for flat profiles – only an upper bound could be determined for  $D_b$  and  $D_c$  and thus the MCMC sampling continued down to  $P_{min}$ ). Values for ( $P_{min}$ ,  $P_{max}$ ) are: ( $-13$ ,  $-11$ ), ( $-15$ ,  $-11$ ), ( $-15$ ,  $-11$ ), ( $0,1$ ) at 810 °C and ( $-11.5$ ,  $-9.5$ ), ( $-14$ ,  $-10$ ), ( $-14$ ,  $-10$ ), ( $0,1$ ) at 1000 °C for  $\log_{10}(D_a)$ ,  $\log_{10}(D_b)$ ,  $\log_{10}(D_c)$ , and edge concentration, respectively. Step sizes were set to be 5 % of the parameter space (0.1, 0.2, 0.2, 0.05 for  $\log_{10}(D_a)$ ,  $\log_{10}(D_b)$ ,  $\log_{10}(D_c)$ , and edge concentration, respectively). Acceptance rate was generally within 20 – 25 %.

Due to the poorly-defined diffusion profiles at all timesteps along **b** and early timesteps along **c**, the MCMC sampling produces a wide range in  $D_b$  and  $D_c$  (see supplementary figures of posterior distributions). In these circumstances, the best-fit values for  $D_b$  and  $D_c$  as determined by the MCMC sampler are not particularly meaningful. Therefore, we fix these parameters, guided by the posterior distributions, and then repeat the least-squares minimization to find the best-fit values of  $D_a$  and edge concentration. Since there is no evidence for a temporal change in  $D_b$ , and the posterior distribution for  $D_b$  is narrower in the final timestep, we set  $D_b$  as the upper bound on the region of  $\pm 1$  sigma on the posterior MCMC distributions for the final timestep – this provides a reasonable estimate of the upper bound of  $D_b$ . For  $D_c$ , at 1000 °C there is a large spread in sampled values for the first two timesteps – for these timesteps the upper bound of the region of  $\pm 1$  sigma of the posterior distribution was chosen. As a diffusion profile along **c** develops, a best-fit value becomes clearer at 2 and 4 h. For these timesteps, the value for  $D_c$  was selected as the mean of the

posterior distribution. At 810 °C, a best-fit value for  $D_c$  is only visible in the final timestep (40 h). Since there is no evidence for a temporal change, the best-fit value from the final timestep is used. For this last timestep, measurements with  $E||c$  show a clear best-fit value and so the mean is used. Measurements with  $E||a$  show a bimodal distribution (Figure S3), with the lower  $D_c$  peak extending to unreasonably slow values ( $<10^{-14}$  m<sup>2</sup>/s); for these distributions we select the upper bound of the region of  $\pm 1$  sigma of the posterior distribution, which coincides with the higher  $D_c$  peak. See plots of posterior distributions in the supplement for clarity. The effect of changing  $D_b$  and  $D_c$  ultimately does not cause an appreciable change in calculated  $D_a$  or edge concentration (in supplementary figures of posterior distributions, compare dashed versus red lines).

### 3. Results

#### 3.1. Defect structure of starting material

The spectra show absorption peaks related to  $Mg^{2+}$  vacancies (lower wavenumbers, between 3100 and 3400) and  $Si^{4+}$  vacancies (high wavenumbers, between 3400 and 3700). As found in other studies (Lemaire et al., 2004; Beran and Libowitzky, 2006), the peaks are largest with  $E||a$  and  $E||c$  and so we focus our attention on these (Fig. 2). The peak at 3232 cm<sup>-1</sup> is thought to signify  $2H^+$  charge-balanced by a  $Mg^{2+}$  vacancy [Mg] (Lemaire et al., 2004); the peaks at 3329, 3359 cm<sup>-1</sup> are a doublet associated with a  $Mg^{2+}$  vacancy charge-balanced by  $H^+$  and trivalent ion ( $Fe^{3+}$ ,  $Cr^{3+}$ ,  $Al^{3+}$ ) substituting on a metal site [triv] (Berry et al., 2007); the peaks at 3524 and 3573 cm<sup>-1</sup> are a doublet created by  $2H^+$  coupled with  $Si^{4+}$  vacancy and  $Ti^{4+}$  on a metal site [Ti] (Fig. 3, Berry et al., 2005). The [Ti] peaks overlap with several smaller peaks which are likely associated with  $Si^{4+}$  vacancies [Si] (Lemaire et al., 2004; Berry et al., 2005). The [triv] peaks are seen with  $E||a$  and  $E||c$  and make up 45 % of the total peak area (summing over all peaks with  $E||a$  and  $E||c$ ). The [Mg] peak makes up 30 % of the area, followed by the [Ti] peaks which make up 20 %, and the [Si] peaks, which make up 5 % (Fig. 3).

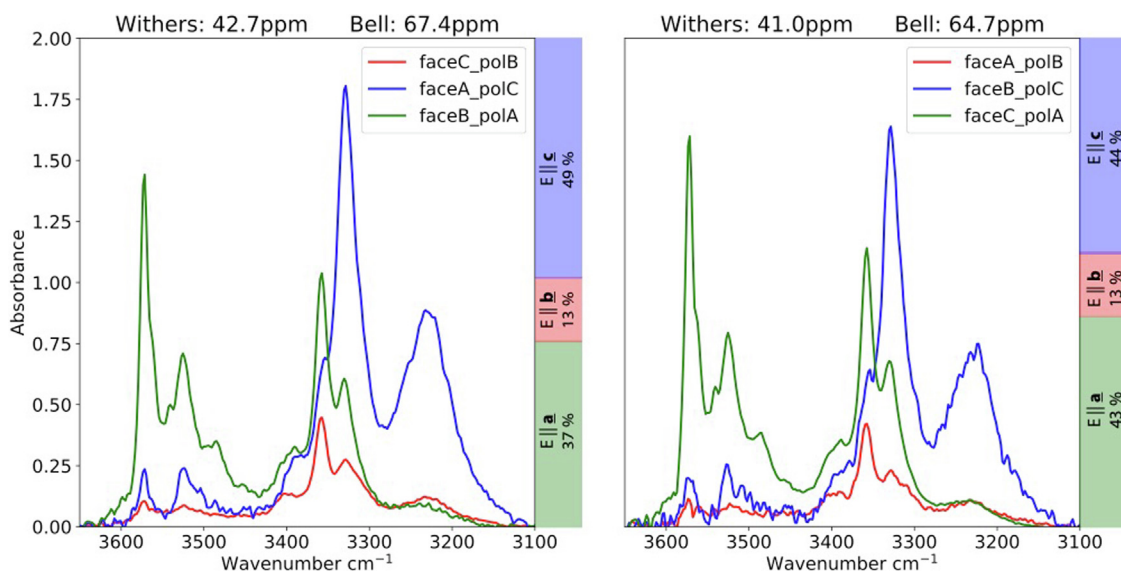


**Fig. 2.** Spectra taken in the centre of each face before dehydration. For each point, spectra are taken with the polarizer in both orthogonal crystallographic directions within the measurement plane (e.g. faceA\_polB and faceA\_polC are taken on face **a** (100), with  $E||b$  [010] and  $E||c$  [001]). Total peak area is calculated as the sum of areas with each polarization direction, and then converted to H<sub>2</sub>O using the Withers et al., 2012 and Bell et al., 2003 calibrations. For each polarization direction, there are two possible faces to measure, so we calculate total water using both sets of faces (left vs right plot) and find good agreement. Bars to the right of each graph show proportion of total peak area for each set of faces contributed from each polarization direction.

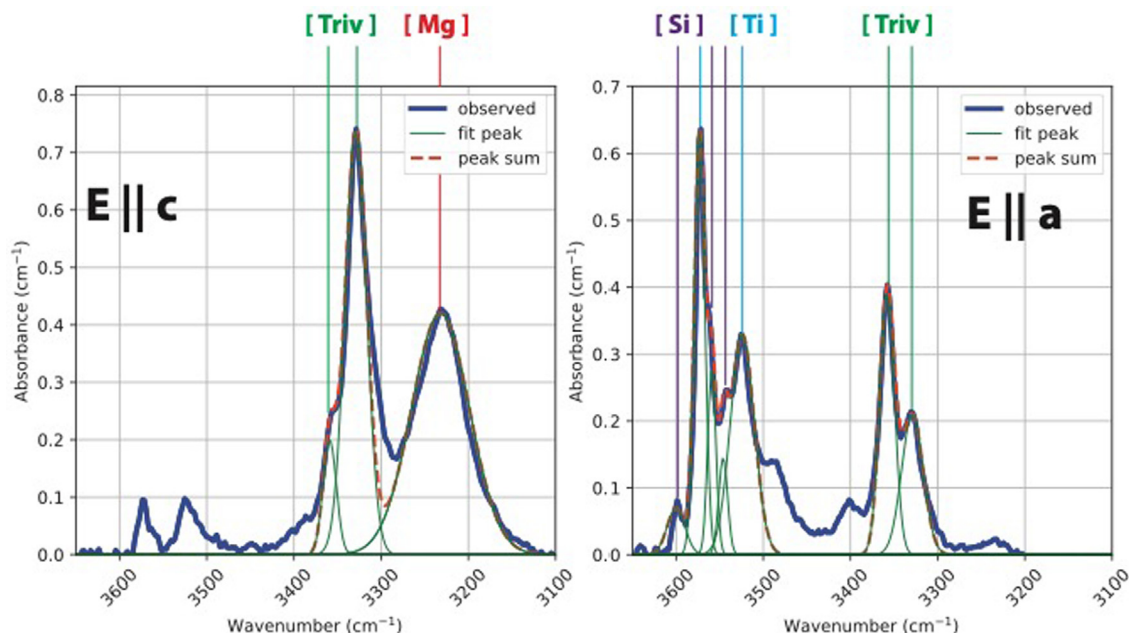


**Fig. 3.** Example spectra for block 2 after two hours of heating at 1000 °C with the electric polarization parallel to **a** and **c**. The [Triv] peak is the only one to be seen clearly with both polarization directions. Bold blue lines show measured spectra, thin green lines show individual modelled peaks, red dashed line shows sum of all individual modelled peaks.

An initial, exploratory experiment of 30 min of heating at 810 °C yielded very little water loss, but did smooth out some variation in the initial profiles. Since a diffusion profile did not clearly develop, the profiles generated at 30 min could not be modelled for diffusivity. Instead, these profiles were used as the initial profiles for subsequent dehydration. A comparison of the initial and 30-minute peak-specific profiles can be found in the supplement (Figure S4).

### 3.2. Dehydration

We observe water loss in experiments at both 810 °C and 1000 °C, which is clearly dominated by diffusion along **a** (Figs. 4 and 5). At both temperatures, diffusivity along **a** is  $\sim 1$  order of magnitude slower than the proton-polaron rate at the start of the time series experiments, and decreases by  $\sim$  half an order of magnitude over the course of the experiments (Figs. 6 and 7). This is seen for all defects, which have the same diffusivity within uncertainty. An exception is the [triv] defect which begins at a slower rate than the other defects at 810 °C (5 h, supplementary data table), although by 8 h it has the same diffusivity as the other defects.

On the other hand, at 1000 °C, diffusivity along **c** appears to increase between two and four hours (Fig. 6). At 810 °C there is no indication that  $D_c$  increases over time, although given the large range in sampled parameter space at early time-steps, the data do not rule it out (Fig. 6).

The concentration profile along **b** remains flat throughout the experiments at both temperatures, and so there is a large uncertainty on  $D_b$  (Fig. 4, Fig. 5). Particularly at short time-steps, the upper bound on  $D_b$  is more clearly defined than the lower bound. For many time-steps there is a negative trade-off between  $D_b$  and  $D_a$  (Fig. 5), which arises because the profile along **a** is measured with the beam parallel to the **b** axis. Higher  $D_b$  (and more water loss along **b**) causes the profile along **a** to be lower and so  $D_a$  must be lower to achieve the same central  $H_2O$  concentration (see Ferriss et al., 2018 for further details).

At all time-steps there is a positive trade-off between the edge concentration and  $D_a$  (Fig. 5). This arises because a lower edge concentration (boundary condition) creates a higher driving force for diffusion and so  $D_a$  must be lower to achieve the same central  $H_2O$  concentration. This is important because it means that studies which fix the edge concentration at zero (e.g. Ferriss et al., 2018) will underestimate the diffusivity responsible for generating the profile.

We estimate two bulk  $H^+$  Arrhenius relationships for  $D_a$ , one for the start and one for the end of the experiments (Fig. 7). Since the diffusivity is the same within uncertainty for all defects, this bulk diffusivity is equivalent to the peak-specific diffusivities. For each time-step, we calculate the average posterior distribution for bulk peaks with  $E||a$  and  $E||c$ , weighted by total peak area (see fig. S7). Since there is only data for two temperatures defining the Arrhenius relationship, we calculate the uncertainty on the activation energy ( $E_a$ ) and pre-exponential factor ( $D_0$ ) by performing a weighted linear regression through the distributions at 810 °C and 1000 °C (for both the start and end of experiments). We use the python package 'scipy.optimize.curve\_fit' (Virtanen et al., 2020) with the y-axis as the natural log of diffusivity, x-axis as  $1e4/T$  ( $T$  in units of K), and sigma given by the 68 % confidence interval on the posterior distribution. The values and 1 sigma uncertainties on  $E_a$  and  $D_0$  are  $182 \pm 20$  kJ/mol and  $10^{-2.94 \pm 0.85}$  for the start and  $154 \pm 7$  kJ/mol and  $10^{-4.63 \pm 0.31}$  for the end. Note that these uncertainties are highly correlated (as indicated by high values of the off-diagonals of the covariance matrix – see fig S8) and that needs to be considered when using uncertainty in the Arrhenius parameters to estimate uncertainty in diffusivity. These uncertainties do not consider possible changes in slope outside of the range of temperatures studied and so caution should be used when extrapolating these Arrhenius laws to higher and lower temperatures. However, we note the close agreement between our Arrhenius relationships and that in Ferriss et al., 2018, which was based on data up to temperatures of 1200 °C.

Since the profiles along **b** and **c** become clearer over time, we calculate an Arrhenius law using the final time-step at both 810

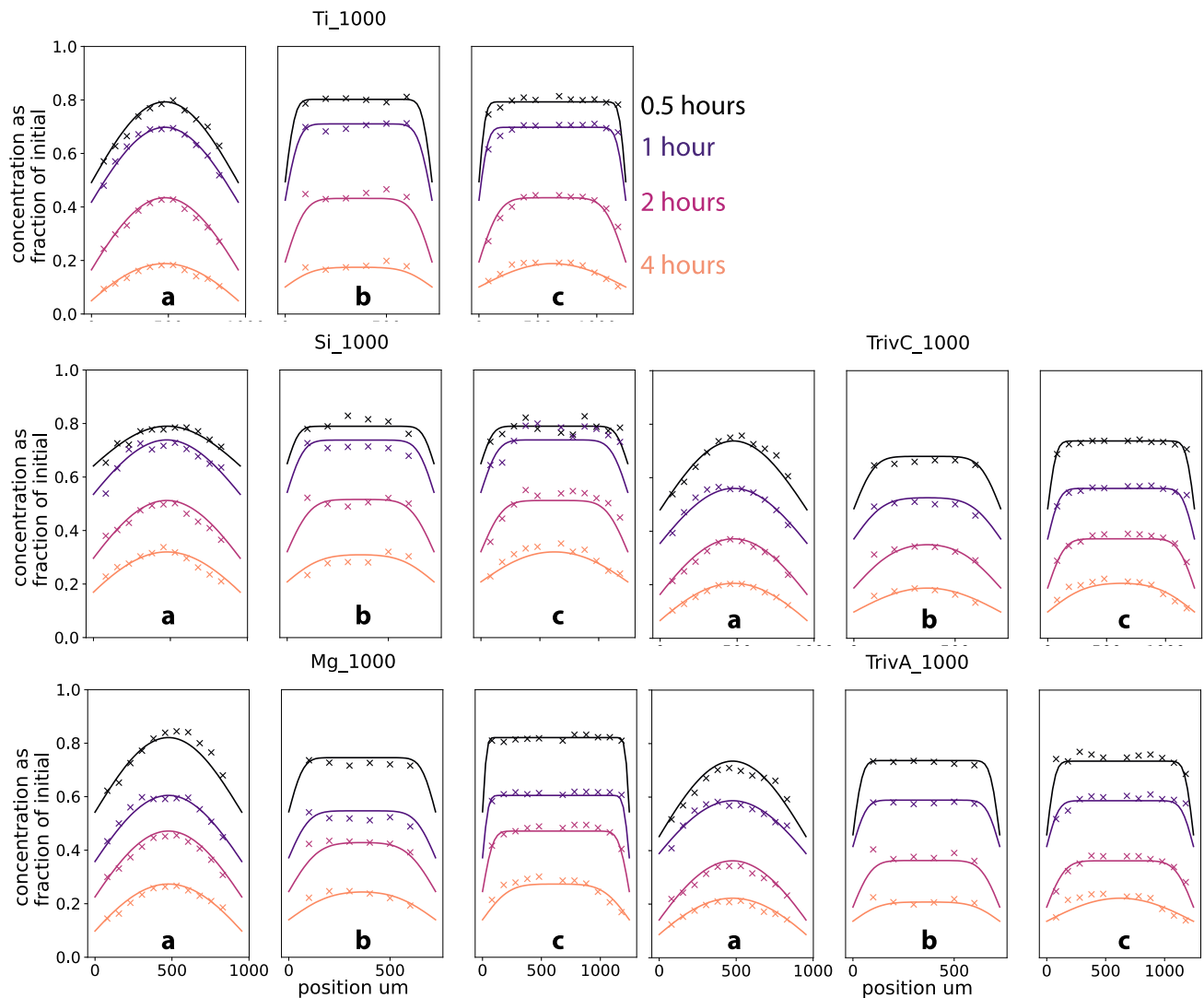


**Fig. 4.** Series of dehydration profiles along **a**, **b** and **c** during dehydration at 1000 °C after 0.5, 1, 2, and 4 h. Profiles shown for all modelled defects (Fig. 3). Curves are generated using the whole block model (Ferriss et al., 2015) with parameters determined by MCMC analysis (all values in supplementary data table, two examples shown in Fig. 5). Modelled profiles (lines) extend from rim to rim of crystal, data (crosses) are measured at finite distance from crystal rim.

and 1000 °C. Uncertainties in Arrhenius parameters are larger than for  $D_a$ , as expected from the larger spread in the MCMC posterior distributions (Fig. 6).  $E_a$  and  $D_0$  are  $243 \pm 76$  kJ/mol and  $10^{-2.35 \pm 3.55}$  m<sup>2</sup>/s for  $D_b$  and  $187 \pm 54$  kJ/mol and  $10^{-4.01 \pm 2.54}$  m<sup>2</sup>/s for  $D_c$ . Covariance matrices are given in figure S8.

The rates that we observe along **a** are approximately one order of magnitude slower than the proton-polaron rate but several orders of magnitude faster than the proton-vacancy rate, and in agreement with the results of a recent study of other Fo ~ 90 olivines from San Carlos and Kilauea Iki (Ferriss et al., 2018).  $D_c$  is 0.6–1.2 log units slower than the proton-polaron mechanism along **c**, although it also aligns with the proton-vacancy mechanism (Fig. 7).

## 4. Discussion

### 4.1. Common peak-specific diffusivity

In agreement with recent studies (Ferriss et al., 2018; Jollands et al., 2019; Thoraval et al., 2019; Li et al., 2022), we find that all defect peaks show diffusion profiles which can be fit with the same

diffusivity (to within 0.25 log units, supplementary data table). Note that (Thoraval et al., 2019) do find a small difference between diffusivities for high and low wavenumber defects, but these are well within uncertainty, especially given that they have no constraint on the initial H<sub>2</sub>O concentrations for each defect. In contrast, Padrón-Navarta et al. (2014) found for pure forsterite that different defects have distinct diffusivities with differences over three orders of magnitude, far exceeding any reasonable uncertainty. Moreover, the peak-specific diffusivities measured by Padrón-Navarta et al. (2014) are significantly slower than all of the diffusivities we report here. This highlights the importance of Fe for H<sup>+</sup> diffusion in olivine – in pure forsterite, there can be no proton-polaron diffusion and so the diffusivities that Padrón-Navarta et al. (2014) measure are closer to the true diffusivity of Si and metal vacancies. In Fe-bearing olivines, the proton-polaron diffusion mechanism can occur, and since it is orders of magnitude faster than the inherent defect-specific diffusivities, it dominates the water loss. H<sup>+</sup> must react out of its defect site in order to diffuse via the proton-polaron mechanism, so the apparent diffusivities that are expressed in our diffusion profiles are not true diffusivities, but a combination of diffusion and reaction (Ferriss et al.,

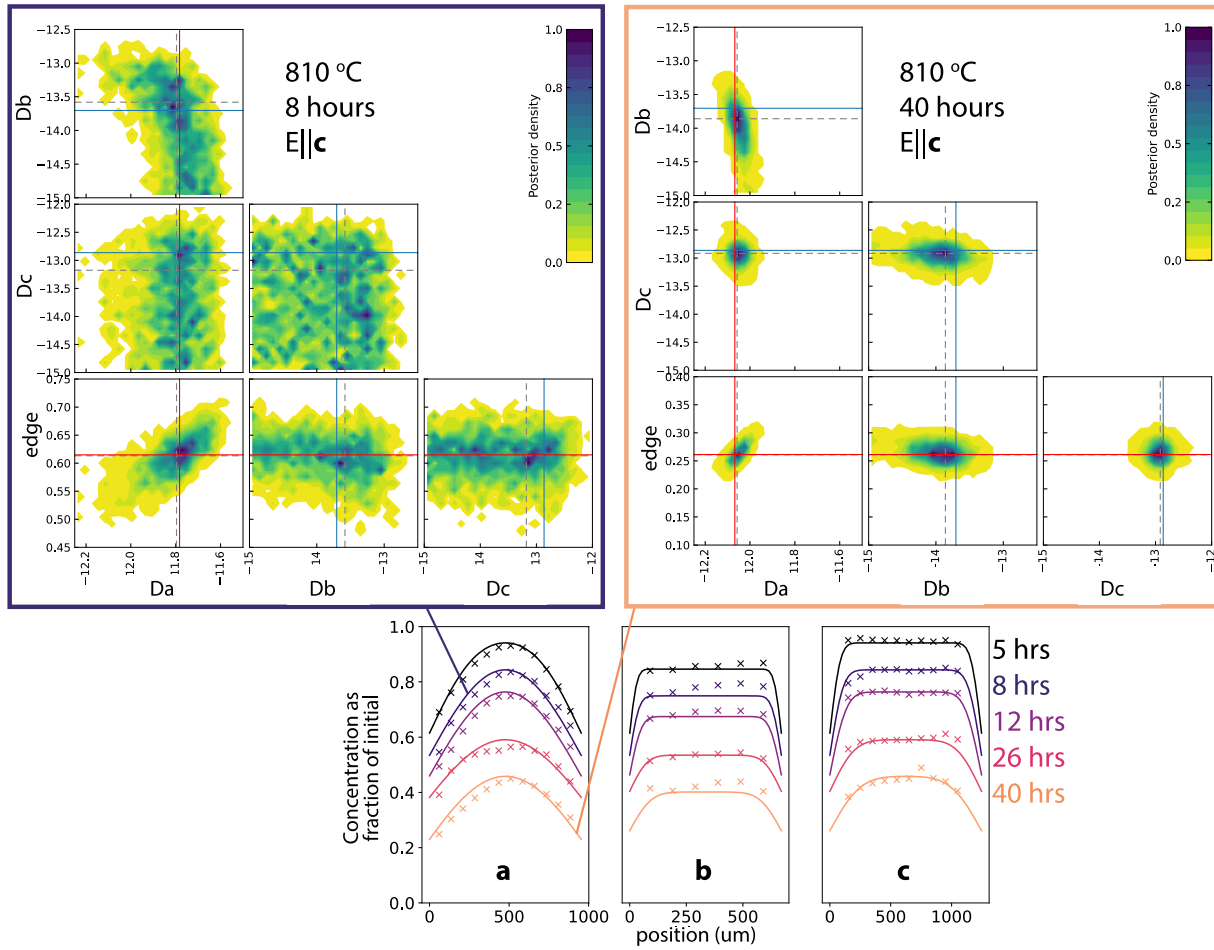
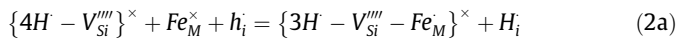


**Fig. 5.** Examples of posterior distributions from MCMC sampling for 8 and 40 h of dehydration at 810 °C. Note positive correlation between  $D_a$  and edge concentration, and negative correlation between  $D_a$  and  $D_b$ . Dashed lines show best-fit values output by MCMC sampling. Solid blue lines show values chosen for  $D_b$  and  $D_c$  based on these posterior distributions. Solid red lines show subsequent best-fit values for  $D_a$  and edge concentration after fixing  $D_b$  and  $D_c$  to chosen values. See text for further details. Note that over time as diffusion profiles develop and the edge concentration becomes more clearly defined, the uncertainty on parameters decreases. Panel below shows profiles being fit in MCMC sampling above (sum of all peaks with  $E||c$ , 810 °C). Plots of MCMC posterior distributions for all profiles (peak-specific, both temperatures) can be found in the supplement.

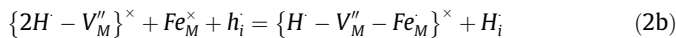
2018; Jollands et al., 2019; Thoraval et al., 2019). Furthermore, the similarity in peak-specific diffusivities that we observe suggests that the reaction constants are similar for all defects, that is,  $H^+$  is equally able to react out of any defect site.

We propose that these reactions require  $Fe^{2+}$  occupying a metal site near a  $H^+$  defect ([triv], [Ti], [Si], [Mg]). For all defects, the  $H^+$  reacts with this  $Fe^{2+}$  to form  $Fe^{3+}$ :

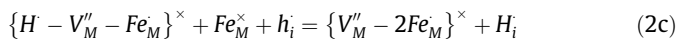
[Si]:



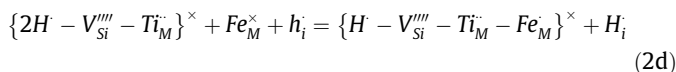
[Mg]:



[triv]:



[Ti]:



These reactions are written in Kröger-Vink notation (Kröger and Vink, 1956), in which curly brackets  $\{\}$  denote a complex point

defect, subscript indicates the site location (M = octahedrally coordinated metal site or Si = tetrahedral silicon site), and superscript indicates the charge (neutral:  $\times$ , positive:  $\cdot$ , negative:  $\prime$ ). For example,  $Ti_M^{\times}$  references a  $Ti^{4+}$  located on a metal vacancy with an overall charge of +2.  $V_{Si}^{''''}$  is a Si vacancy with a charge of -4. Note that the product of the reaction for [Mg] is the [triv] defect – the [triv] defect could be seen as an intermediate step in the full dehydration of the [Mg] defect. In equation 2d, considerations of energy minimization suggest that the Ti may move from Mg to Si site (Brodholt and Refson, 2000; Hermann et al., 2005), but it is unclear if this would occur on the timescales of these experiments and for simplicity we keep it in the same site (M) before and after reaction (Jollands et al., 2016 find Ti diffusivities of  $< 10^{-13} \text{ m}^2/\text{s}$  at 1300 °C). A polaron (electron hole) is denoted by  $h^{\cdot}$ , which can be thought of as the excess charge on a  $Fe^{3+}$  (relative to normal metal site occupancy). After reacting out of its defect site, the  $H^+$  is then activated to diffuse rapidly via the proton-polaron mechanism, charge-balanced by a counter flow of polarons:



Or, since the polarons are thought to be associated with the excess charge of  $Fe^{3+}$ , this can be written as:





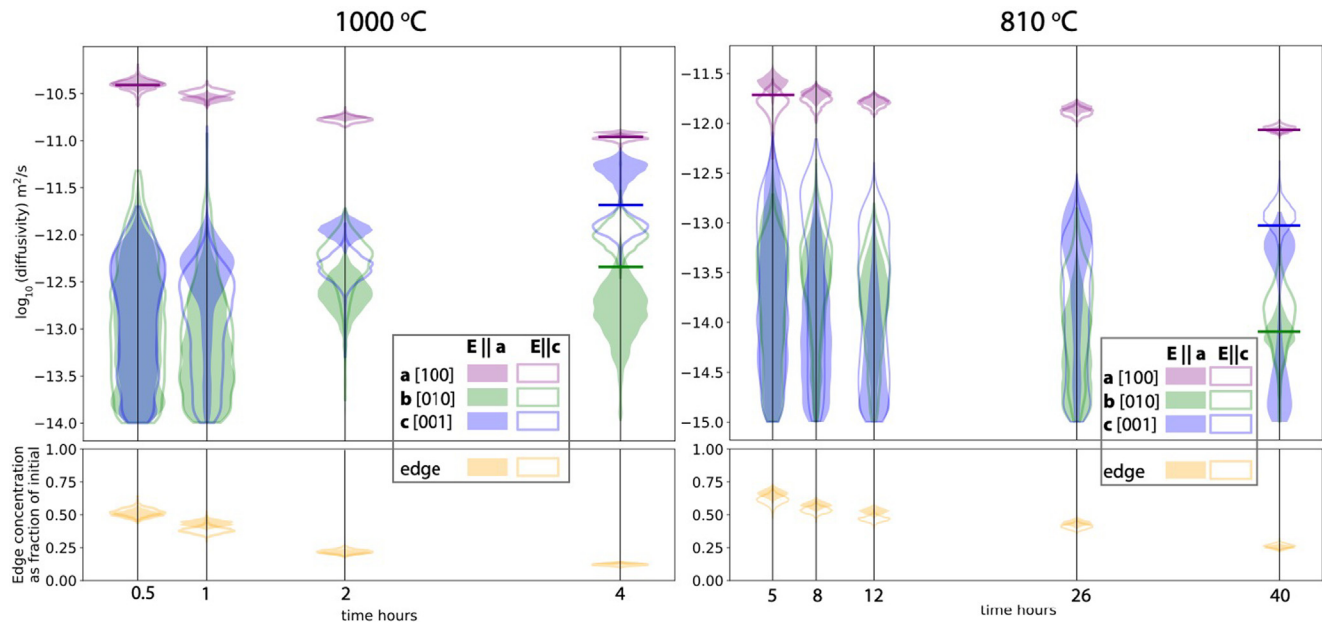


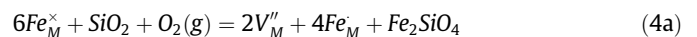
**Fig. 6.** Diffusivity and edge concentration over time for 810 (right) and 1000 °C (left), shown as violin plots of MCMC sampled posterior distributions. Solid colors show results from fitting bulk peaks with polarizer parallel to  $\underline{a}$  ( $E||\underline{a}$ ); outlines show polarizer parallel to  $\underline{c}$  ( $E||\underline{c}$ ). Horizontal lines at first and final times for  $D_a$  and final times for  $D_b$  and  $D_c$  indicate values used for Arrhenius relationships.  $D_b$  and  $D_c$  are poorly constrained at the start, which is why Arrhenius relationships for  $D_b$  and  $D_c$  are only calculated for the final time.  $D_a$  decreases over time by  $\sim$  half a log unit for both temperatures. At 1000 °C,  $D_c$  appears to speed up between 2 and 4 h.

#### 4.2. Temporal changes in apparent diffusivity

We observe that the apparent diffusivity along  $\underline{a}$  slows down by  $\sim 0.5$  log units over the course of the experiments (4 h at 1000 °C, 40 h at 810 °C). Since the true proton-polaron diffusivity should be time-invariant, it follows that this apparent decrease must be related to the reaction step. In all of the reactions written above, the key reactant allowing the reaction to proceed is  $\text{Fe}^{2+}$  (or  $\text{Fe}_M^\times$  in equations 2–3). As dehydration progresses,  $\text{Fe}^{2+}$  is oxidized to  $\text{Fe}^{3+}$  and Ferriss et al. (2018) proposed that this (very slight) build-up of  $\text{Fe}^{3+}$  could slow down the reactions. Jollands et al. (2019) argued that there was essentially an infinite source of  $\text{Fe}^{2+}$  relative to  $\text{H}^+$ . However, for an olivine with  $F_o \sim 90$ , only 1/10 metal sites will be occupied by Fe, which is less than one Fe per unit cell (the unit cell contains four formula units – 8 metal sites). Consider the reactions above: only the [triv] defect fully dehydrates after one reaction with  $\text{Fe}^{2+}$ . The other defects, which contain multiple  $\text{H}^+$  ions, require more than one reaction to lose all of their  $\text{H}^+$ . When the first dehydration reaction step occurs and the nearby  $\text{Fe}^{2+}$  is oxidized to  $\text{Fe}^{3+}$ , the remaining  $\text{H}^+$  in that defect will be trapped until another  $\text{Fe}^{2+}$  (which is likely more than a unit cell away) diffuses to the defect. The diffusivity of Fe-Mg exchange in olivine at 1000 °C is  $\sim 10^{-17} \text{ m}^2/\text{s}$  (Dohmen and Chakraborty, 2007), many orders of magnitude lower than  $\text{H}^+$  diffusion. However, for length scales on the order of the unit cell (5–10 Å), the time scales implied by these diffusivities are less than a second, therefore local rearrangement of Fe during the experiments should be possible.

It appears that at 1000 °C the diffusivity along  $\underline{c}$  increases over time (Fig. 6). This increase along  $\underline{c}$  has not been found in previous studies (although the profiles in Ferriss et al. (2019) do not rule it out), and we do not have a good explanation for it, or why it is absent at 810 °C. Focusing first on an explanation for the increase in  $D_c$  at 1000 °C, it is possible that the relatively oxidizing conditions of the furnace set by gas mixing (NNO + 1.2) promotes the

formation of vacancies and  $\text{Fe}^{3+}$  at the olivine-gas interface, as described in Equation 3 of Nakamura and Schmalzried (1983):



In a 1 atm. gas mixing furnace, it is unclear where the  $\text{SiO}_2$  could come from, but the reaction could instead be written as:



which would create FeO at the crystal-gas interface. The proton-vacancy diffusivity should be independent of the vacancy concentration. However, the diffusivity of Fe-Mg exchange is enhanced by increasing vacancy concentrations (Dohmen and Chakraborty, 2007), so it is possible that  $\text{H}^+$  defects have a faster supply of  $\text{Fe}^{2+}$  along  $\underline{c}$  (since Fe-Mg diffusion is 6 times greater along  $\underline{c}$  than along  $\underline{a}$ ), which allows for faster reactions. Thus, oxidation at the crystal edge could lead to a greater vacancy concentration and so higher rate of Fe diffusion along  $\underline{c}$  with time, which could result in an increase in  $D_c$  with time.

The absence of an increase in  $D_c$  over time at 810 °C could be due to the higher activation energy of the proton vacancy compared to the proton polaron mechanism (258 kJ/mol versus 130 kJ/mol – Mackwell and Kohlstedt, 1990; Demouchy and Mackwell, 2003; Demouchy and Mackwell, 2006; Jollands et al., 2021). At 810 °C, the proton vacancy mechanism  $||\underline{c}$  is 3.4 log units slower than proton polaron  $||\underline{a}$ , while at 1000 °C it is only 2.4 log units slower.

#### 4.3. Edge concentration

Despite the lack of  $\text{H}^+$  in the gas surrounding the olivines during experiments, models which fit the diffusion profiles well require a non-zero boundary condition, that is, the  $\text{H}_2\text{O}$  concentration does not reach zero at the crystal edge, nor can it be reasonably extrapolated to zero. In our fitting procedure we treat the edge concentration as a free parameter and find the best-fit value at each



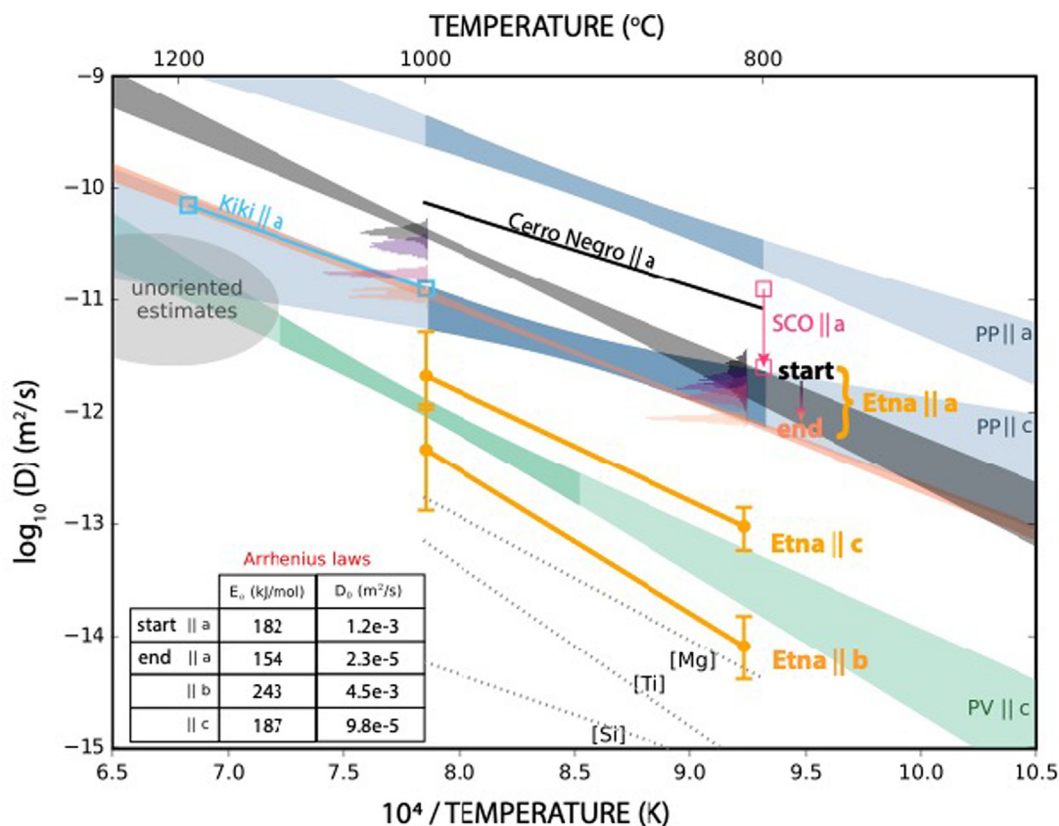


**Fig. 7.** Arrhenius diagram for H diffusion in olivine. Blue and green shaded region shows  $\pm 1$  sigma confidence envelopes for previous measurements of proton-polaron rate (PP – Kohlstedt & Mackwell 1998) and proton-vacancy rate (PV – Demouchy & Mackwell 2003) during hydration of San Carlos olivine. Darker shading on these envelopes indicates the region where there are data constraints. Calculation of error envelopes for PP, PV and this study is detailed in figure S9. Note that envelopes are for  $D_{\text{exchange}}$ , not for  $D_H$  or  $D_{V,Me}$  (see section 1 for more details). Etna Fall Stratified results (this study) determined by summing posterior distributions for bulk peaks with  $E||a$  and  $E||c$ , weighted by total peak area (see fig. S7). Gray to peach graded colors show decrease in  $D_a$  for Etna Fall Stratified over time. Arrhenius relationships at start and end for  $D_a$  shown by  $\pm 1$  sigma confidence envelopes. Since distributions for  $D_b$  and  $D_c$  are less clear (Fig. 6), only the mean and  $\pm 1$  sigma for the final time-step are shown (orange). Black dotted lines show peak-specific measurements from dehydration of synthetic forsterite (Padrón-Navarta et al. (2014). Blue line shows measurements on natural Kilauea Iki olivines (Ferriss et al., 2018); pink arrow at 810 °C shows range of measurements of  $D_a$  on San Carlos olivine, which slowed down over time (Ferriss et al., 2018). Note that subsequent reanalyses of profiles in Ferriss et al. (2018) shows large uncertainty due to FTIR data – see supplement. Estimates for bulk  $H^+$  diffusivity in unoriented MI-bearing olivines shown by grey ellipse (Portnyagin et al., 2008; Mironov et al., 2015; Chen et al., 2011; Gaetani et al., 2012). Activation energies ( $E_a$ ) and pre-exponential factors ( $D_0$ ) for our Arrhenius laws are provided in the inset table.

time which minimizes the misfit. Over the course of the experiments, the best-fit edge concentration decreases from 50 % to 12 % of the initial concentration at 1000 °C and from 64 % to 25 % at 810 °C. If the edge concentration is fixed at zero, the fits are significantly worse and the best-fit diffusivity along **a** decreases markedly – for profiles after 8 h at 810 °C, the diffusivity along **a** changes from  $10^{-11.72}$  m²/s if the edge concentration is a free parameter to  $10^{-12.58}$  m²/s if the edge is fixed at zero (Figure S5).

The development of non-zero boundary conditions during dehydration has been found in other experimental studies, as well as natural samples (Ferriss et al., 2018; Reyness et al., 2018; Jollands et al., 2019; Newcombe et al., 2020). Newcombe et al. (2020) found non-zero edge concentrations in  $H_2O$  profiles for natural olivines from Seguam, Kilauea, and Cerro Negro. However, while this is logical for these natural crystals, which are surrounded by a host magma containing dissolved  $H_2O$ , for our laboratory experiments, the crystals are in a completely dry environment.

Non-zero edge concentrations in lunar glass beads have been modelled by a combination of diffusion and evaporation from the bead surface (Fogel and Rutherford, 1995; Saal et al., 2008). However, the timescales investigated for the lunar beads were far shorter ( $\sim 300$  s) than those of our experiments, and it seems unlikely that  $H_2O$  evaporation is rate-limiting on timescales of hours in a furnace at 810 or 1000 °C and 1 atm.

Another possibility is that the oxidation reaction (Equation 4b) creates FeO and  $Fe^{3+}$  at the olivine-gas interface, changing the local kinetics such that  $H_2O$  loss at the interface is hindered, and thereby pinning the  $H_2O$  edge concentration to values above zero.

Alternatively, the non-zero edge concentration could be understood within the coupled reaction–diffusion scheme described above. If the local arrangement of defects becomes less favourable for reactions as dehydration progresses, the reactions will be slowest at the crystal edge where water loss is highest. With a spatially varying reaction rate (highest in the centre, lowest at the edges), this could cause an apparent locking of  $H^+$  at the crystal edge. Thus, the same underlying phenomena creating the decrease in apparent diffusivity may be responsible for non-zero concentrations of  $H_2O$  at the crystal edge.

There are some similarities between the profiles we observe and those modelled by Thoraval and Demouchy (2014). They model the combined effect of simultaneous proton-polaron and proton-vacancy mechanisms, assuming that the two processes do not interact, and that there are finite ‘reservoirs’ of  $H^+$  that can diffuse via each mechanism. Initially, a proton-polaron diffusion profile develops along **a** with edge concentrations equal to the amount of  $H^+$  stored in the proton-vacancy reservoir (which can never be accessed by the proton-polaron mechanism in their model). Once the proton-polaron reservoir is used up, the proton-vacancy mech-

anism takes over and the anisotropy becomes fast along  $\bar{c}$  (see their Fig. 6). The modelling approach in Thoraval and Demouchy (2014) is largely informed by hydration experiments, in which a clear transition occurs between an initial fast proton-polaron mechanism, followed by the proton-vacancy mechanism. This transition makes sense for hydration experiments since the proton-polaron mechanism for hydration requires  $\text{Fe}^{3+}$ , which exists in such small quantities in olivine that it can be entirely consumed. Once the proton-polaron mechanism exhausts the available  $\text{Fe}^{3+}$ , it can no longer occur, and so diffusion proceeds at the proton-vacancy rate. However, as originally proposed by Ferriss et al. (2018), this may not be the case during dehydration, since  $\text{Fe}^{2+}$  exists in high enough quantities that it is always available to facilitate the proton-polaron mechanism. Instead of the abrupt transition modelled in Thoraval and Demouchy (2014) with entirely separate reservoirs for proton-polaron and proton-vacancy mechanisms, we favour a more gradual transition for dehydration. At each time-step, the edge concentration may represent a reservoir of  $\text{H}^+$  that is temporarily unable to diffuse via the proton-polaron mechanism, i.e. defects that are less favourably located with respect to  $\text{Fe}^{2+}$ . Over time, the size of this reservoir decreases (and the edge concentration decreases) as  $\text{Fe}^{2+}$  diffuses short distances to the 'locked'  $\text{H}^+$  and reacts with it, enabling the  $\text{H}^+$  to diffuse once again via proton-polaron.

#### 4.4. Comparison to other studies on natural olivines

There is a small but growing number of hydrogen diffusion experiments on natural olivines. Because of the differences between hydration and dehydration experiments in terms of defect availability (Ferriss et al., 2018), we focus our comparison on other dehydration experiments. Natural olivines from Cerro Negro, Kilauea and San Carlos all show the same fast diffusion along  $\bar{a}$  that we see for the Etna Fall Stratified olivines (Ferriss et al., 2018; Barth et al., 2019). Within uncertainties (see supplement for re-analysis of profiles from Ferriss et al., 2018), there is broad agreement between these studies, with diffusivity along  $\bar{a}$  lying between the proton-polaron rate and roughly an order of magnitude slower. Therefore, as originally proposed by Ferriss et al., 2018, the fast rates and orientation of anisotropy suggest that natural olivines dehydrate via the proton-polaron mechanism, with reactions between defect sites slowing down apparent diffusivity from the true proton-polaron rate.

An exception to this agreement is a recent paper by Li et al. (2022), which shows fastest diffusion along  $\bar{c}$ , and with diffusivity along  $\bar{a}$  significantly slower than the studies mentioned above ( $\sim 10^{-13}$  at 1000 °C). These authors argue that dehydration is occurring via the proton-vacancy mechanism. Understanding the differences between these studies is crucial for interpreting  $\text{H}_2\text{O}$  concentration profiles in natural olivines. Below, we first describe some differences in terms of experimental protocols, and then discuss the effect that olivine composition may have on  $\text{H}^+$  diffusivity.

##### 4.4.1. Effect of experimental procedure

Ferriss et al. (2018) found that apparent bulk diffusivity for the San Carlos olivine began at near proton-polaron rates, nearly an order of magnitude faster than Kilauea Iki (Ferriss et al., 2018) or Etna Fall Stratified (this study). The San Carlos olivines were experimentally hydrated before dehydration, which would have likely resulted in a close association of  $\text{H}^+$  defects and  $\text{Fe}^{2+}$  at the start of dehydration, allowing fast reactions. Under these conditions, the reactions were not rate limiting at the start of the experiments and so the apparent diffusivity is closer to the true proton-polaron diffusivity. Neither Kilauea nor Etna olivines were experimentally hydrated before dehydration.

Li et al., 2022 also experimentally hydrated their San Carlos olivines, however they did this for long enough timescales and high enough temperatures to add more water than the natural olivines would have originally contained (and more water than Ferriss et al., 2018 added). In order to accommodate such high water concentrations, a significant number of vacancies must have been created in their olivines. They find fastest diffusion along  $\bar{c}$ , and with diffusivities in line with the proton-vacancy mechanism. Fast diffusion along  $\bar{c}$  is at odds with studies based on both experiments (Ferriss et al., 2018; Barth et al., 2019; Jollands et al., 2019) and observed  $\text{H}_2\text{O}$  zonation in natural olivines (Le Voyer et al., 2014; Thoraval et al., 2019; Newcombe et al., 2020). One explanation for the striking discrepancies between Li et al., 2022 and other studies (including experiments also on San Carlos olivines by Ferriss et al., 2018) is that hydrating the samples to such a great extent changed the defect structure enough to alter the reaction rates between defect sites and thus slow down the apparent proton-polaron diffusivity to below the diffusivity of the proton-vacancy mechanism. Unfortunately, the concentration of  $\text{H}_2\text{O}$  in the olivine after hydration and prior to dehydration was not reported in Li et al. (2022). It was likely not measured, and was instead a free parameter that they fit in their diffusion model. From their Fig. 7 the highest absorption area is  $\sim 36 \text{ cm}^{-2}$ , significantly higher than that in the experiments of Ferriss et al. (2018) of  $24 \text{ cm}^{-2}$ . Furthermore, since they do not measure the initial  $\text{H}_2\text{O}$  concentration and their shortest dehydration experiment was two hours, the initial absorption area may well have been higher than  $36 \text{ cm}^{-2}$  initially. Dehydration may have transitioned from an initial phase of fast water loss along  $\bar{a}$ , which was not observed, to a later stage of fast water loss along  $\bar{c}$ .

Going forwards, the effect of any experimental conditions prior to dehydration should be carefully considered, and if available, naturally hydrous olivines are preferable to experimentally hydrated olivines for interpreting naturally produced diffusion profiles. Furthermore, it is crucial that  $\text{H}_2\text{O}$  concentrations prior to dehydration be measured and reported. Ideally, future studies would be conducted on large hydrous natural olivine, although since these samples are rare, clinopyroxene crystals might provide a suitable and more readily available proxy for these experiments (Ferriss et al., 2016; Lloyd et al., 2016). Further dehydration studies on natural clinopyroxenes may be a good direction for future work. In addition, future studies targeting the effect of experimental hydration protocol on subsequent dehydration diffusivities would be extremely useful.

##### 4.4.2. Effect of forsterite, $\text{H}_2\text{O}$ , and $f\text{O}_2$

We now return to the question laid out in the introduction: how does the olivine forsterite content,  $\text{H}_2\text{O}$  concentration, and the  $f\text{O}_2$  of last equilibration affect the  $\text{H}^+$  diffusivity? We focus our discussion here on naturally hydrous olivines, due to the effects of experimental hydration discussed above. The olivines in this study from the Fall Stratified eruption of Etna are the most hydrous magmatic olivines for which  $\text{H}^+$  diffusivity data exist, with 42 or 66 ppm  $\text{H}_2\text{O}$  (depending on calibration – see Fig. 2). The close agreement between our results and those for Kilauea Iki olivines (Ferriss et al., 2018), which had considerably lower  $\text{H}_2\text{O}$  concentrations ( $\sim 20$  ppm) and  $f\text{O}_2$  (NNO-0.45) but similar forsterite (Table 2), suggests that at least within the range of pressure, temperature, and time explored so far, the effect of  $\text{H}_2\text{O}$  and  $f\text{O}_2$  on  $\text{H}^+$  diffusivity is negligible. An important caveat is that the olivines in these studies were surrounded by a  $\text{CO-CO}_2$  gas mixture, not a melt. It is possible that if the experimental olivines were surrounded by a melt that could host changes in the valence state of its cations such as Fe in response to  $f\text{O}_2$ , this could affect the diffusivity. For example, Shea and Ruth (2022) show that for diffusion of major and minor

**Table 2**H<sub>2</sub>O, *f*O<sub>2</sub> and forsterite of experimentally dehydrated magmatic olivines.

Sample	H <sub>2</sub> O concentration (ppm) (calibration of Withers et al., 2012)	<i>f</i> O <sub>2</sub> Δ NNO	Fo %
San Carlos <sup>1</sup>	3 ppm (9 ppm after annealing)	NNO (during annealing)	88
Kilauea Iki <sup>1</sup>	12 ppm	NNO – 0.45	86
Cerro Negro <sup>2</sup>	6 ppm	NNO + 0.25	79
Etna Fall-Stratified <sup>3</sup>	42 ppm	NNO + 1.2	90

<sup>1</sup> Ferriss et al. (2018)<sup>2</sup> Barth et al. (2019)<sup>3</sup> This study.

elements, experiments with a surrounding melt demonstrate faster diffusivities than those with solid–solid couples. However, in the study by Ferriss et al. (2018), the H<sup>+</sup> diffusivity obtained from modelling a diffusion profile in a natural melt-hosted olivine from Kilauea was in agreement with the Arrhenius law determined by dehydrating Kilauea olivines using a gas-mixing furnace, suggesting that the surrounding melt did not affect the diffusion significantly. Since this is based on only one study, and two olivines, further work targeting the effect of the host medium on olivine diffusivity would be beneficial.

Of the experimentally dehydrated magmatic olivines, the highest diffusivity is exhibited by those from Cerro Negro (Barth et al., 2019). These olivines do not have remarkable *f*O<sub>2</sub> or H<sub>2</sub>O concentration compared to the typical range of magmatic olivines, but have significantly lower forsterite (79), suggesting that the forsterite content is the dominant control on the diffusivity during dehydration of natural olivine. The Cerro Negro olivines also did not show a decrease in apparent bulk H<sup>+</sup> diffusivity over time, supporting the hypothesis that the availability of Fe<sup>2+</sup> plays a key role in the temporal evolution of apparent diffusivity.

## 5. Conclusions

One of the promising applications of H<sup>+</sup> diffusion in olivine is as a chronometer of magma ascent during volcanic eruptions. For this purpose, uncertainties in magma decompression rate are dominated by large uncertainties in the diffusivity, in part due to unknown effects of olivine chemistry on H<sup>+</sup> diffusivity. Our results indicate that the forsterite content has the largest effect on apparent diffusivity of H<sup>+</sup> in olivine, surpassing any effect of H<sub>2</sub>O or *f*O<sub>2</sub> within the range for typical magmatic systems. However, there are still relatively few studies that directly target the control of olivine composition on diffusivity, and studies which experimentally hydrate olivines prior to dehydration should be considered with caution when applied to modelling naturally produced diffusion profiles. Further studies on the effects of composition on H<sup>+</sup> diffusivity for both olivine and clinopyroxene would be useful.

Unlike experiments on Fe-free olivines (Padrón-Navarta et al., 2014), we find that defects in natural, Fe-bearing olivines all exhibit the same apparent H<sup>+</sup> diffusivity. This can be understood within the framework of a coupled diffusion–reaction process, whereby Fe-mediated reactions liberate H<sup>+</sup> from its bonded location within any defect site and allow it to diffuse via the proton–polaron mechanism (Ferriss et al., 2018; Jollands et al., 2019). A common diffusivity for all defects is an important finding as it may validate the use of methods that can only measure bulk water, such as SIMS. Many olivines in natural samples are too small or do not have enough H<sub>2</sub>O to show well-resolved FTIR spectral peaks when doubly polished; for such samples, SIMS may be the only method able to measure H<sup>+</sup> diffusion profiles (e.g. Le Voyer et al., 2014; Newcombe et al., 2017).

In closing, the use of an ‘apparent diffusivity’ to incorporate the combined effects of diffusion plus reaction may be sufficient for first order modelling of H<sup>+</sup> diffusion profiles. Future work could

use the data presented in this paper to develop a coupled reaction–diffusion model, which may shed light on both the non-zero edge concentration and the temporal variations in apparent diffusivity.

## Declaration of Competing Interest

The authors declare that they have no known competing financial interests or personal relationships that could have appeared to influence the work reported in this paper.

## Acknowledgements

This work was supported by US National Science Foundation, grant numbers EAR-1524542 and EAR-1731784. We would like to thank Alberto Malinverno for his guidance on the MCMC methods, Mike Jollands, Philipp Ruprecht and Paul Wallace for their comments on an early version of the manuscript, and Elizabeth Ferriss for her help with the FTIR collection and processing (see <https://github.com/EFerriss/Pynams>). We are thankful to Louise Bolge for help with the laser, Dave Walker for aiding with experiments, and Silvio Rotolo for providing the sample. We are grateful for thoughtful reviews from three anonymous reviewers which vastly improved the manuscript.

## Appendix A. Supplementary material

The supplementary material includes (1) supplementary figures and figure captions, as referenced in the text, (2) posterior distributions from MCMC fitting for all profiles (peak-specific, at both temperatures, for all times), (3) results from refitting profiles in Ferriss et al., 2018 using the MCMC approach in this study. The supplementary data table includes Laser ablation ICP-MS data for both olivine blocks and best-fit values for anisotropic diffusivity and edge H<sub>2</sub>O concentration for peak-specific profiles.

Supplementary material to this article can be found online at <https://doi.org/10.1016/j.gca.2022.11.009>.

## References

- Bai, Q., Kohlstedt, D.L., 1992. Substantial hydrogen solubility in olivine and implications for water storage in the mantle. *Nature* 357, 672–674.
- Barth, A., Newcombe, M., Plank, T., Gonnermann, H., Hajimirza, S., Soto, G.J., Saballos, A., Hauri, E., 2019. Magma decompression rate correlates with explosivity at basaltic volcanoes—Constraints from water diffusion in olivine. *Journal of Volcanology and Geothermal Research* 387, 106664.
- Barth, A., 2021. Volatiles and ascent rates of explosive basaltic volcanism. Columbia University.
- Bell, D.R., and Rossman, G.R., 1992. Water in Earth's mantle: the role of nominally anhydrous minerals. *Science*, v. 255, p. 1391–1397.
- Bell, D.R., Rossman, G.R., Maldener, J., Endisch, D., Rauch, F., 2003. Hydroxide in olivine: A quantitative determination of the absolute amount and calibration of the IR spectrum. *Journal of Geophysical Research: Solid Earth* 108.
- Beran, A., Libowitzky, E., 2006. Water in Natural Mantle Minerals II: Olivine, Garnet and Accessory Minerals. *Reviews in Mineralogy and Geochemistry* 62, 169–191.
- Beran, A., Putnis, A., 1983. A model of the OH positions in olivine, derived from infrared-spectroscopic investigations. *Physics and Chemistry of Minerals* 9, 57–60.



- Beran, A., 1969. Über OH-gruppen in Olivin: Österreich Akademie Des Wissenschaften.
- Berry, A.J., Hermann, J., O'Neill, H.S.C., Foran, G.J., 2005. Fingerprinting the water site in mantle olivine. *Geology* 33, 869–872.
- Berry, A.J., O'Neill, H.S.C., Hermann, J., Scott, D.R., 2007. The infrared signature of water associated with trivalent cations in olivine. *Earth and Planetary Science Letters* 261, 134–142.
- Blanchard, M., Ingrin, J., Balan, E., Kovács, I., Withers, A.C., 2017. Effect of iron and trivalent cations on OH defects in olivine. *American Mineralogist* 102, 302–311.
- Brodholt, J.P., Refson, K., 2000. An ab initio study of hydrogen in forsterite and a possible mechanism for hydrolytic weakening: *Journal of Geophysical Research: Solid Earth* 105, 18977–18982.
- Cassidy, Mike et al., 2018. Controls on explosive-effusive volcanic eruption styles. *Nature commun.* 9 (1), 1–16.
- Chen, Yang et al., 2011. The rate of water loss from olivine-hosted melt inclusions. *Contrib. Mineral. Petrol.* 162.3, 625–636.
- Cottrell, M., Del Carlo, P., Pompilio, M., Vezzoli, L., 2005. Explosive eruption of a picrite: The 3930 BP subplinian eruption of Etna volcano (Italy). *Geophysical Research Letters* 32, 1–4.
- Cubillos, P., Harrington, J., Lored, T.J., Lust, N.B., Blecic, J., Stemm, M., 2016. On correlated-noise analyses applied to exoplanet light curves. *The Astronomical Journal* 153, 3.
- Demouchy, S., Mackwell, S., 2003. Water diffusion in synthetic iron-free forsterite. *Physics and Chemistry of Minerals* 30, 486–494.
- Demouchy, S., Mackwell, S., 2006. Mechanisms of hydrogen incorporation and diffusion in iron-bearing olivine. *Physics and Chemistry of Minerals* 33, 347–355.
- Demouchy, S., Jacobsen, S.D., Gaillard, F., Stem, C.R., 2006. Rapid magma ascent recorded by water diffusion profiles in mantle olivine. *Geology* 34, 429–432.
- Dohmen, R., Chakraborty, S., 2007. Fe-Mg diffusion in olivine II: Point defect chemistry, change of diffusion mechanisms and a model for calculation of diffusion coefficients in natural olivine. *Physics and Chemistry of Minerals* 34, 409–430.
- Dohmen, R., Becker, H.-W., Chakraborty, S., 2007. Fe-Mg diffusion in olivine I: experimental determination between 700 and 1,200 °C as a function of composition, crystal orientation and oxygen fugacity. *Physics and Chemistry of Minerals* 34, 389–407.
- Faul, U.H., Cline II, C.J., David, E.C., Berry, A.J., Jackson, I., 2016. Titanium-hydroxyl defect-controlled rheology of the Earth's upper mantle. *Earth and Planetary Science Letters* 452, 227–237.
- Ferriss, E., Plank, T., Walker, D., Nettles, M., 2015. The whole-block approach to measuring hydrogen diffusivity in nominally anhydrous minerals. *American Mineralogist* 100, 837–851.
- Ferriss, E., Plank, T., Walker, D., 2016. Site-specific hydrogen diffusion rates during clinopyroxene dehydration. *Contributions to Mineralogy and Petrology* 171, 1–24.
- Ferriss, E., Plank, T., Newcombe, M., Walker, D., Hauri, E., 2018. Rates of dehydration of olivines from San Carlos and Kilauea Iki. *Geochimica et Cosmochimica Acta* 242, 165–190.
- Fogel, R.A., Rutherford, M.J., 1995. Magmatic volatiles in primitive lunar glasses: I. FTIR and EPMA analyses of Apollo 15 green and yellow glasses and revision of the volatile-assisted fire-fountain theory. *Geochimica et Cosmochimica Acta* 59, 201–215.
- Gennaro, E., Paonita, A., Iacono-Marziano, G., Moussallam, Y., Pichavant, M., Peters, N., Martel, C., 2020. Sulphur behaviour and redox conditions in etnean magmas during magma differentiation and degassing. *Journal of Petrology*.
- Hermann, J., O'Neill, H.S.C., Berry, A.J., 2005. Titanium solubility in olivine in the system TiO<sub>2</sub>-MgO-SiO<sub>2</sub>: no evidence for an ultra-deep origin of Ti-bearing olivine. *Contributions to Mineralogy and Petrology* 148, 746–760.
- Jarosewich, E., Nelen, J.A., Norberg, J.A., 1980. Reference Samples for Electron Microprobe Analysis. *Geostandards Newsletter* 4, 43–47.
- Jollands, M.C., Hermann, J., O'Neill, H.S.C., Spandler, C., Padrón-Navarta, J.A., 2016. Diffusion of Ti and some Divalent Cations in Olivine as a Function of Temperature, Oxygen Fugacity, Chemical Potentials and Crystal Orientation: *Journal of Petrology* 57, 1983–2010.
- Jollands, M.C., Kempf, E., Hermann, J., Müntener, O., 2019. Coupled inter-site reaction and diffusion: rapid dehydration of silicon vacancies in natural olivine. *Geochimica et Cosmochimica Acta* 262, 220–242.
- Jollands, M.C., O'Neill, H.S.C., Berry, A.J., Le Losq, C., Rivard, C., and Hermann, J., 2021. A combined Fourier transform infrared and Cr K-edge X-ray absorption near-edge structure spectroscopy study of the substitution and diffusion of H in Cr-doped forsterite: *European journal of mineralogy*, v. 33, p. 113–138.
- Kamenetsky, V.S., Pompilio, M., Métrich, N., Sobolev, A.V., Kuzmin, D.V., Thomas, R., 2007. Arrival of extremely volatile-rich high-Mg magmas changes explosivity of Mount Etna. *Geology* 35, 255–258.
- Karato, S., 1990. The role of hydrogen in the electrical conductivity of the upper mantle. *Nature* 347, 272–273.
- Kelley, K.A., Plank, T., Ludden, J., Staudigel, H., 2003. Composition of altered oceanic crust at ODP Sites 801 and 1149. *Geochemistry, Geophysics, Geosystems* 4.
- Kohlstedt, D.L., Mackwell, S.J., 1998. Diffusion of Hydrogen and Intrinsic Point Defects in Olivine. *Zeitschrift für Physikalische Chemie* 207, 147–162.
- Kröger, F.A., Vink, H.J., 1956. Relations between the concentrations of imperfections in crystalline solids. *Solid state physics*, Elsevier 3, 307–435.
- Le Voyer, M., Asimow, P.D., Mosenfelder, J.L., Guan, Y., Wallace, P., Schiano, P., Stolper, E.M., Eiler, J.M., 2014. Zonation of H<sub>2</sub>O and F concentrations around melt inclusions in olivines. *Journal of Petrology* 55, 685–707.
- Lemaire, C., Kohn, S.C., Brooker, R.A., 2004. The effect of silica activity on the incorporation mechanisms of water in synthetic forsterite: a polarised infrared spectroscopic study. *Contributions to Mineralogy and Petrology* 147, 48–57.
- Li, Y. (Will), Mackwell, S.J., and Kohlstedt, D.L., 2022. Diffusion rates of hydrogen defect species associated with site-specific infrared spectral bands in natural olivine: *Earth and Planetary Science Letters*, v. 581, p. 117406, doi:10.1016/j.epsl.2022.117406.
- Lloyd, A.S., Ferriss, E., Ruprecht, P., Hauri, E.H., Jicha, B.R., Plank, T., 2016. An assessment of clinopyroxene as a recorder of magmatic water and magma ascent rate. *Journal of Petrology* 57, 1865–1886.
- Mackwell, S.J., Kohlstedt, D.L., 1990. Diffusion of hydrogen in olivine: implications for water in the mantle: *Journal of Geophysical Research: Solid Earth* 95, 5079–5088.
- Matveev, S., O'Neill, H.S.C., Ballhaus, C., Taylor, W.R., and Green, D.H., 2001. Effect of silica activity on OH- IR spectra of olivine: implications for low- $\alpha$  SiO<sub>2</sub> mantle metasomatism: *Journal of Petrology*, v. 42, p. 721–729.
- Mironov, Nikita et al., 2015. Quantification of the CO<sub>2</sub> budget and H<sub>2</sub>O-CO<sub>2</sub> systematics in subduction-zone magmas through the experimental hydration of melt inclusions in olivine at high H<sub>2</sub>O pressure. *Earth and Plan. Sci. Lett.* 425, 1–11.
- Nakamura, A., Schmalzried, H., 1983. On the nonstoichiometry and point defects of olivine. *Physics and Chemistry of Minerals* v. 10, 27–37.
- Newcombe, M.E., Asimow, P.D., Ferriss, E., Barth, A., Lloyd, A.S., Hauri, E., and Plank, T.A., 2017. Water-in-Olivine Magma Ascent Chronometry: Every Crystal is a Clock, in AGU Fall Meeting Abstracts.
- Newcombe, M.E., Plank, T., Barth, A., Asimow, P., Hauri, E., 2020. Water-in-olivine magma ascent chronometry: Every crystal is a clock. *Journal of Volcanology and Geothermal Research*, 106872.
- Novella, D., Jacobsen, B., Weber, P.K., Tyburczy, J.A., Ryerson, F.J., Du Frane, W.L., 2017. Hydrogen self-diffusion in single crystal olivine and electrical conductivity of the Earth's mantle. *Scientific Reports* 7, 1–10.
- Padrón-Navarta, J.A., Hermann, J., O'Neill, H.S.C., 2014. Site-specific hydrogen diffusion rates in forsterite. *Earth and Planetary Science Letters* 392, 100–112.
- Portnyagin, Maxim et al., 2008. Experimental evidence for rapid water exchange between melt inclusions in olivine and host magma. *Earth and Plan. Sci. Lett.* 272 (3–4), 541–552.
- Reynolds, J., Jollands, M., Hermann, J., and Ireland, T., 2018. Experimental constraints on hydrogen diffusion in garnet: Contributions to mineralogy and petrology, v. 173, p. 1–23.
- Saal, A.E., Hauri, E.H., Cascio, M.L., Van Orman, J.A., Rutherford, M.C., Cooper, R.F., 2008. Volatile content of lunar volcanic glasses and the presence of water in the Moon's interior. *Nature* 454, 192–195.
- Shea, T., and Ruth, D., 2022. Cation diffusion in magmatic olivine and the 'melt problem,' in Goldschmidt.
- Ter Braak, C.J.F., Vrugt, J.A., 2008. Differential evolution Markov chain with snooker updater and fewer chains. *Statistics and Computing* 18, 435–446.
- Thoraval, C., Demouchy, S., 2014. Numerical models of ionic diffusion in one and three dimensions: application to dehydration of mantle olivine. *Physics and Chemistry of Minerals* 41, 709–723.
- Thoraval, C., Demouchy, S., Padrón-Navarta, J.A., 2019. Relative diffusivities of hydrous defects from a partially dehydrated natural olivine. *Physics and Chemistry of Minerals*, 1–13.
- Virtanen, P. et al., 2020. SciPy 1.0: fundamental algorithms for scientific computing in Python. *Nature Methods* 17, 261–272.
- Withers, A.C., Bureau, H., Raepsaet, C., Hirschmann, M.M., 2012. Calibration of infrared spectroscopy by elastic recoil detection analysis of H in synthetic olivine. *Chemical Geology* 334, 92–98.
- Yoshino, T., Matsuzaki, T., Yamashita, S., Katsura, T., 2006. Hydrous olivine unable to account for conductivity anomaly at the top of the asthenosphere. *Nature* 443, 973–976.